

© 2020 IEEE. Personal use of this material is permitted. Permission from IEEE must be obtained for all other uses, in any current or future media, including reprinting/republishing this material for advertising or promotional purposes, creating new collective works, for resale or redistribution to servers or lists, or reuse of any copyrighted component of this work in other works.

# Direct estimation of global longitudinal strain from echocardiograms using a logarithm-scaled Fourier magnitude correlation

Brett A. Meyers, Melissa C. Brindise, Vivek Jani, Shelby Kutty, Pavlos P. Vlachos

**Abstract**— We present a new algorithm – the logarithmic-transform correlation (LTC) method – for measuring global longitudinal strain (GLS) and global longitudinal strain rate (GLSr) from 2D echocardiograms. In contrast to conventional GLS computation methods, our approach does not require boundary segmentation and regularization. The algorithm was benchmarked against conventional GLS methods using synthetic left ventricle (LV) ultrasound images generated to represent five different ischemia conditions each on five different ultrasound imaging systems. LV GLS and GLSr measurement error was assessed as a function of contrast-to-noise (CNR) ratio using mean absolute error (MAE) and root-mean-square error (RMSE). Our algorithm showed strong agreement to the ground truth for both GLS ( $R^2 = 0.91$ ) and GLSr ( $R^2 = 0.85$ ). Conventional GLS algorithms showed less agreement for GLS ( $R^2 = 0.7$ ) and GLSr ( $R^2 = 0.7$ ). In addition, our method was unaffected by CNR. A 200% improvement in both MAE and RMSE was observed compared to conventional GLS algorithms. A clinical demonstration was performed using a 54-subject cohort of pediatric patients (20 subjects with cardiomyopathy, 34 controls). Our method distinguished between normal and abnormal left ventricular function with an AUC = 0.85, a 10% improvement over conventional GLS algorithms.

**Index Terms**—Echocardiography, global longitudinal strain, image registration, speckle tracking.

## I. INTRODUCTION

Echocardiography is a non-invasive imaging method used for cardiac health examinations because it is affordable, accessible, and easy to use [1]. Measurements of left ventricle (LV) morphology (end-systolic volume [ESV], end-diastolic volume [EDV], stroke volume [SV]), hemodynamics (peak E-wave filling velocity), function (ejection fraction [EF], and cardiac output [CO]) are obtained from imaging studies [1], [2]. In clinical practice, EF is a standard metric for evaluation of LV function [3], assessment of systolic heart failure [4]–[6], tracking outcomes in implantable device surgeries [5], [7] and cardiac resynchronization therapy (CRT) [6]. However, EF is

susceptible to large intra- and inter-observer variation [3], [8], is load- and age-dependent, and does not characterize diastolic function.

In contrast to EF, strain and strain rate measurements from Speckle Tracking Echocardiography (STE) have been shown to provide information on diastolic function, while maintaining better sensitivity and differentiation in assessing LV function and heart failure [9]. B-mode STE estimates myocardial tissue length changes using cross-correlation algorithms from digital imaging correlation (DIC) to track the photo-acoustic speckle patterns generated by cardiac muscle fibers as ultrasound pressure waves pass through tissue and blood [10], [11]. Strain and strain rate are estimated by tracking hand-drawn LV boundaries and comparing local changes in the distance between speckle patterns through time, across an entire cardiac cycle. This technique can be used with apical long-axis (ALAX) imaging to obtain estimates of Global Longitudinal Strain (GLS) and Global Longitudinal Strain Rate (GLSr) [12].

Several factors must be considered when performing STE. Firstly, scan quality, including spatial and temporal resolutions, and signal dropout, affect boundary detection and tracking [13]. Secondly, commercial platforms provide a variety of LV shape models, and proper selection requires considerable training to obtain reliable GLS estimates [1]. Thirdly, GLS varies between the layers of heart wall based on current software methods [14]. Fourthly, commercial platforms have differences in both proprietary tracking and post-processing algorithms (including spatial and temporal regularization), which makes cross-platform comparison impossible [1], [15]. These factors, along with user-variability, represent limitations that hinder the establishment of standard ranges for normal and abnormal function [9], [16] for GLS measurements [17]–[19]. This lack of consensus concerning proper definitions has motivated an industry-driven effort to create imaging standardization guidelines but has ultimately led to delays in clinical implementation.

In this work, we present a novel algorithm for direct GLS

Manuscript submitted for review on February 24, 2020. This work was not supported by external funding.

B. A. Meyers and M. C. Brindise are with the School of Mechanical Engineering, Purdue University, West Lafayette, IN, 47907 (e-mail: meyers18@purdue.edu; mbrindis@purdue.edu).

V. Jani and S. Kutty are with the Taussig Heart Center, Johns Hopkins University School of Medicine, Baltimore, MD, 21287 (e-mail: vjani1@jhmi.edu; skutty1@jhmi.edu).

P. P. Vlachos is with the School of Mechanical Engineering and School of Biomedical Engineering, Purdue University, West Lafayette, IN, 47907 (e-mail: pvlachos@purdue.edu).

estimation from echocardiogram recordings, developed to address limitations observed in conventional STE algorithms. Our framework bypasses existing STE limitations including biases due to regional smoothing as well as assumptions on tissue shape and deformation. Instead, the algorithm uses a logarithm-scale basis transform of the magnitude of Fourier-transformed images. We performed GLS and GLSr error analysis using synthetic ultrasound images created as part of the standardization studies [20]. Validation was done using clinical data of normal subjects and patients with cardiomyopathy. We compared results from our algorithm against standard STE algorithms using direct image cross-correlation and Fourier-based cross-correlation.

## II. METHODS

Throughout the cardiac cycle the LV contracts and relaxes, resulting in motion that is complex and three dimensional. However, for echocardiogram scans with sufficient frame rates, out-of-plane motion is negligible, allowing motion to be represented as 2D. This motion is composed of a planar translation  $\vec{T}$  and deformation gradient tensor  $\mathbf{F}$  which can be used to relate the pixel intensities between any two consecutive scan frames,  $I_n$  and  $I_{n+1}$ , at pixel coordinates  $(x, y)$ ,

$$I_{n+1}(x, y) = \mathbf{F}I_n(x, y) + \vec{T} = \begin{bmatrix} \mathbf{a}_{11} & \mathbf{a}_{12} \\ \mathbf{a}_{21} & \mathbf{a}_{22} \end{bmatrix} I_n(x, y) + \begin{bmatrix} t_1 \\ t_2 \end{bmatrix}. \quad (1)$$

$\mathbf{F}$  is homogeneous and is related to the displacement gradient tensor  $\nabla \mathbf{u}$  through the expression,

$$\mathbf{F} = \mathbf{I} - \nabla \mathbf{u}, \quad (2)$$

where  $\mathbf{I}$  is the identity matrix. Lagrange strain,  $\boldsymbol{\varepsilon}$ , can be expressed as a function of  $\nabla \mathbf{u}$  when motion and deformation are small, such that,

$$\boldsymbol{\varepsilon} = \frac{1}{2} (\nabla \mathbf{u} + \nabla \mathbf{u}^T), \quad (3)$$

and the strain when  $\boldsymbol{\varepsilon}$  is aligned in the direction of the length change is equivalent to,

$$\varepsilon = \frac{l - l_0}{l_0}. \quad (4)$$

Therefore,  $\mathbf{F}$  is directly related to strain. In the following sections we derive how strain is directly estimated from the cross-correlation of two consecutive frames based on these equations.

### A. Cross-correlation methods

#### 1) Pairwise cross-correlation

Digital image cross-correlation provides a statistical estimate of rigid translation between two images. This estimate is used in applications such as image registration [21], speckle tracking [22], [23], particle image velocimetry (PIV) [24], and DIC [25], [26]. The 2D discrete *spatial cross-correlation* kernel between two images is expressed as,

$$R(x, y) = \sum_{j=-N/2}^{N/2} \sum_{j=-M/2}^{M/2} I_n(i, j) I_{n+1}(x + i, y + j), \quad (5)$$

where  $R(x, y)$  is the correlation plane,  $(i, j)$  are the summation indices for each pixel intensity, and  $N$  and  $M$  are the image

height and width, respectively. Variants of this correlation kernel include sum-of-square-differences (SSD) and sum-of-absolute-differences (SAD). The 2D discrete cross-correlation can be performed in the spectral domain, with the *spectral cross-correlation* written as,

$$R(x, y) = \mathcal{F}^{-1}[\bar{\mathcal{F}}(I_n(x, y))\mathcal{F}(I_{n+1}(x, y))] = \mathcal{F}^{-1}[\bar{F}(u, v)G(u, v)], \quad (6)$$

where  $\mathcal{F}$  is the 2D Fourier transformation (FT),  $F$  and  $G$  are the transformed images, and  $(u, v)$  are the *spectral wave numbers* related to the pixel coordinates.

The affine theorem for Fourier transforms indicates that rotation, stretch, and shear which occur between images will also occur on both the magnitude and phase of the image FT [27]. We can observe how the affine transform contributes to the rigid translation estimate from the cross correlation by replacing  $I_{n+1}$  in Equation 5 with the relationship defined in Equation 1,

$$R(x, y) = \mathcal{F}^{-1}[\bar{\mathcal{F}}(I_n(x, y))\mathcal{F}(\mathbf{F}I_n(x, y) + \vec{T})], \quad (7)$$

which can be written alternatively as,

$$R(x, y) = \iint \bar{F}(u, v)F(u', v')e^{-\frac{j2\pi}{\Delta}(t_1u' + t_2v')} dudv. \quad (8)$$

Here,  $u' = a_{11}u/\Delta - a_{12}v/\Delta$ ,  $v' = a_{22}v/\Delta - a_{21}u/\Delta$ , and  $\Delta = \det(\mathbf{F}) = a_{11}a_{22} - a_{12}a_{21}$ . Equation 8 indicates that the row and column displacements from the correlation plane are translations affected by local displacement gradients. The row and column displacements,  $\Delta r$  and  $\Delta c$ , are therefore written as,

$$\Delta c \cong a_{11}t_1 - a_{12}t_2, \quad \Delta r \cong -a_{21}t_1 + a_{22}t_2. \quad (9)$$

Although the displacement gradients are present in the rigid translation estimates, these gradients are integral to computing GLS in the conventional algorithms. By calculating local translation measurements to track the LV boundary, the gradients compute the overall change in length of the LV boundary, and therefore represent the strain observed through the GLS calculation.

#### 2) Fourier magnitude transforms

Based on Equation 8, it can be reasoned that the components introduced by  $\mathbf{F}$  can be observed independent of  $\vec{T}$  by separating the FT magnitude,  $|F(u, v)|$ , from the phase content. The FT magnitudes of two images can be cross-correlated, where the returned row and column displacements from the cross-correlation plane are a combination of terms from  $\mathbf{F}$  with no contribution from  $\vec{T}$ . This correlation method is therefore considered *translation invariant*. A basis transformation can be used to further decouple terms from  $\mathbf{F}$  and resolve information on rotation and image stretching.

The Fourier-Mellin transform (FMT) is the most well-known FT magnitude transformation, applying a *log-polar* basis change to decouple rotation from isotropic scaling [28]. The FT magnitude image coordinates are changed from the Cartesian  $(u, v)$  coordinates to orthogonal  $(\log \rho, \theta)$  coordinates. In this coordinate system, the shift theorem introduces displacements due to a rotation  $\alpha$  or scale change  $m$  such that [29],

$$F(\log p + \log m, \theta + \alpha). \quad (10)$$

Using cross-correlation of two FT magnitude image pairs, where one image has undergone a uniform rescaling and rotation to produce the second, allows  $\alpha$  and  $m$  to be estimated from the row and column displacements. The *translation invariance* allows rotation and scaling to be estimated reliably [29], even when a shift is present. The FMT works well when scaling is uniform ( $m \propto a_{11} = a_{22}$ ) and rotation occurs without shear ( $\alpha \propto a_{12} = a_{21}$ ). Therefore, this transform will not work reliably when scaling change is anisotropic.

When scaling is anisotropic a *logarithm scale* basis change should be used. Changing the FT magnitude image coordinates from Cartesian  $(u, v)$  to orthogonal  $(\log u, \log v)$  coordinates results in the shift theorem introducing displacements due to horizontal rescaling  $a$  and vertical rescaling  $b$  such that,

$$F(\log(au), \log(bv)) = F(\log u + \log a, \log v + \log b). \quad (11)$$

Rescaling is still reliably estimated although the *translation invariance* allows a shift to be present [30]. This transform does require that rotation and shear be minimized (observed from the terms present in Equation 8. The row and column displacements estimate  $a$  and  $b$  are related to the terms  $a_{11}$  and  $a_{22}$  from  $\mathbf{F}$  through,

$$a_{11} \approx e^{\Delta c}, \quad a_{22} \approx e^{\Delta r} \quad (12)$$

The logarithm scale basis change with FT magnitude cross-correlation can also be used to obtain GLS from our algorithm.

### B. Direct global longitudinal strain estimation algorithm

Our algorithm for computing LV GLS from B-mode ultrasound ALAX scans uses Fourier-based cross-correlation of the *logarithm scale* image FT magnitudes to estimate the stretch that takes place along the length of the ventricle. As long as rotation and shear are assumed negligible (or minimized),  $a_{11}$  and  $a_{22}$  from Equation 12 can replace  $F$  in Equation 2 which can then be used to solve for  $\nabla \mathbf{u}$  such that,

$$\nabla \mathbf{u} = \begin{bmatrix} e^{\Delta c} - 1 & 0 \\ 0 & e^{\Delta r} - 1 \end{bmatrix}. \quad (13)$$

Because most of the deformation in the ALAX scans occurs along the length of the ventricle, we assume GLS occurs predominantly along the vertical direction; thus, GLS can be estimated as,

$$\varepsilon_{GLS} = \frac{l - l_0}{l_0} \approx e^{\Delta r} - 1. \quad (14)$$

A schematic of our proposed algorithm to compute GLS based on the correlation of *logarithm scale* FT magnitudes is provided in Figure 1. The algorithm is composed of two stages – the first stage performs an image registration to minimize shear, rotation, and noise that can corrupt the correlation accuracy, while the second stage performs GLS estimation. The algorithm begins with the user selecting the frames across a single heartbeat (Figure 1a), from peak diastole to peak diastole (R-R interval). Next, three initial points from the first frame in the stack are selected (Figure 1b), corresponding to the LV

apex, the mitral annulus (MA) septal, and the MA lateral positions. These points are tracked between consecutive frames using standard pairwise cross-correlation (Figure 1c). For each frame, the geometric center from the tracked points is computed with the orientation angle from the vertical axis, for a line formed from the MA center to the apex (Figure 1d). Frames are aligned with the geometric center set to the image midpoint. The orientation angle from vertical is corrected. A circular ROI is then resolved from the tracked points for each frame and used to remove tissue signal and noise that occurs outside the LV.

In the second stage, for a pair of sequential registered images,  $t$  and  $t+1$  (Figure 1e), the FT for each image and their FT magnitude is computed. The FT magnitudes are then interpolated from the image grid onto a logarithm-scale grid (Figure 1f). In order to properly estimate the stretch through cross-correlation, the FT logarithm transformed images must be separated into four quarters. This is because the horizontal stretch between the left and right side of the images have the same magnitude but are of opposite sign; the same occurs for the vertical stretch between the top half and bottom half of the images. After the images are separated, each sub-image is filtered [31] and the FT computed. The FT sub-images from the frame pair are then correlated using the *spectral cross-correlation* kernel to provide the row and column displacements  $\Delta r$  and  $\Delta c$  (Figure 1h). A dynamic phase-filtered kernel is applied to the cross-correlation to improve estimate accuracy [32]–[34]. The displacements  $\Delta r$  and  $\Delta c$  are adjusted based on the logarithm-scale grid, becoming  $\Delta r'$  and  $\Delta c'$ . The GLSr between the frame pair is computed using  $\Delta r'$  from (14). Finally, GLSr across each frame pair is integrated in time using 4<sup>th</sup>-Order Runge-Kutta to obtain GLS (Figure 1i). We will hereafter refer to this method as the Logarithm-Transform Correlation (LTC) method.

### C. Speckle tracking strain

This study uses two STE algorithms which employ different correlation kernels to benchmark our LTC method. One algorithm uses the SAD correlation [22], as described by Equation 5, referred to herein as the *Direct Cross-Correlation* or DCC method. The second uses the *spectral cross-correlation*, described by Equation 6, hereafter referred to as the *Fourier Transform Correlation* or FTC method. GLS is computed using local displacement estimates from both algorithms with LV boundary segmentations.

A 64x64 pixel correlation window resolution was used to compute the FTC cross-correlation and a 49x49 correlation window resolution to compute the DCC cross-correlation. Local displacements are computed on an 8x8 grid. Boundary tracking was performed by displacing the segmented boundary of the initial frame based on the displacement field for each frame pair using 4<sup>th</sup>-Order Runge-Kutta. GLS was estimated from the measured change in arc-length between the boundary of the initial frame and the tracked boundary from each frame.

### D. Synthetic ultrasound recordings

Error analysis was performed using synthetic LV ALAX echocardiograms [20], [35] generated for echocardiogram strain measurement standardization studies conducted by the

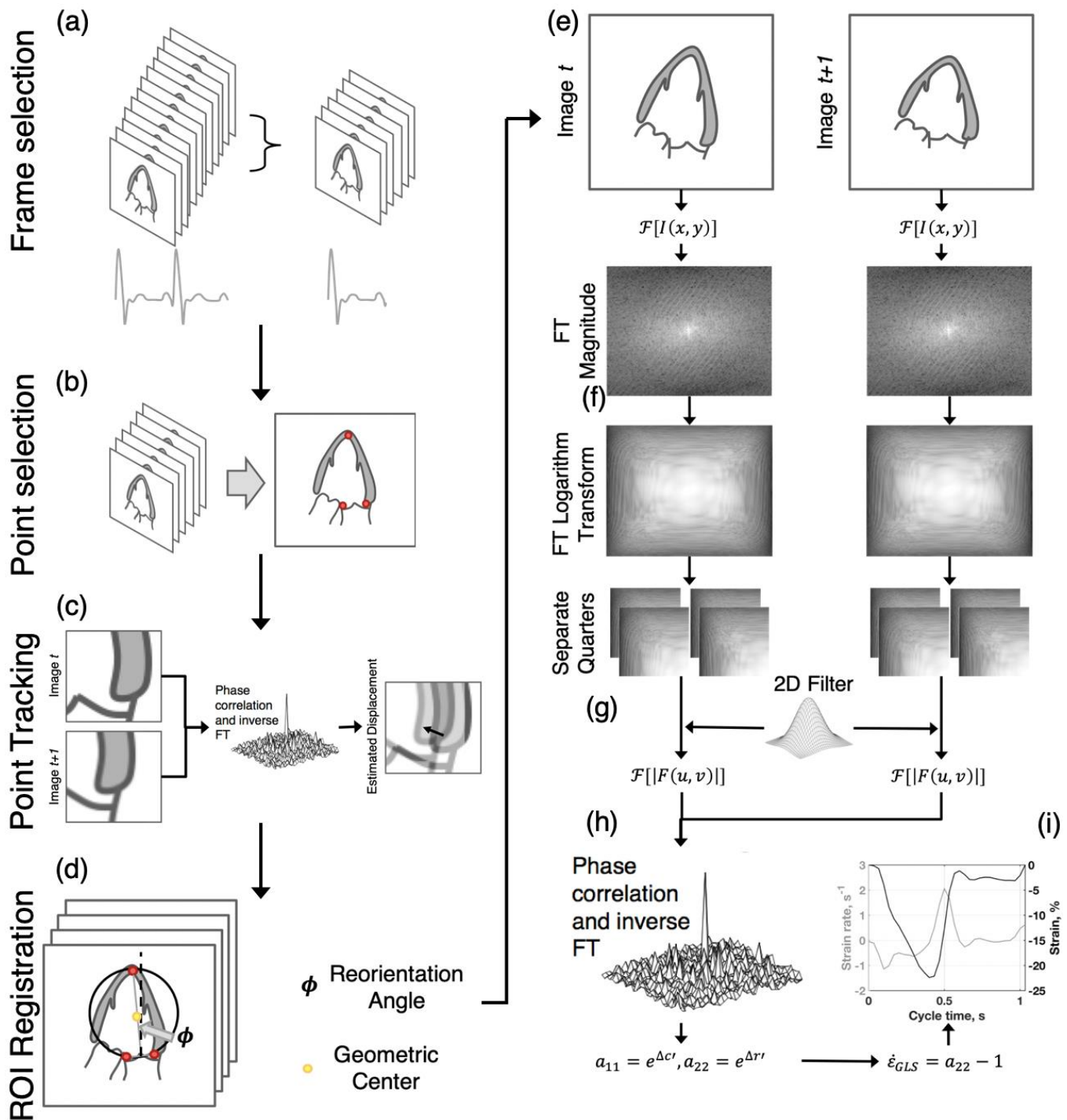


Figure 1: Illustration of the direct longitudinal strain estimation algorithm used to measure global longitudinal strain.

European Association of Cardiovascular Imaging - American Society of Echocardiography Task Force (EACVI-ASE-TF) [15], [36]–[39]. The synthetic datasets were modelled to match five vendor-systems: GE Vivid E9, Hitachi Prosound  $\alpha 7$  CV, Philips iE 33 Vision, Siemens SC2000, and Toshiba Artida. For each system, a non-ischemic, left anterior descending artery (LAD) distal occlusion, LAD proximal occlusion, left circumflex artery (LCX) occlusion, and right coronary artery (RCA) occlusion ischemic state were modelled [40]. Ground truth LV boundaries, displacements, and corresponding strains for each dataset were included with the synthetic images.

Measured-to-expected plots for GLS and GLSr were used to analyze the strength of association between each modality and ground truth. More robust methods were expected to have a fit quality near  $R = 1.0$ , a linear region slope near 1.0, and a bias intercept near 0.0. Mean absolute error (MAE) and root-mean-square error (RMSE) for GLS and GLSr were quantified as a function of contrast to noise ratio (CNR). CNR was defined as the ratio of L2-norm of the tissue signal to L2-norm of the signal inside the LV [41]. Error quantities were normalized by the peak GLS or peak GLSr from all non-ischemic cases, regardless of machine.

### E. Clinical imaging

Clinical capabilities of the LTC method as compared to conventional STE methods were demonstrated using a cohort of pediatric patients with confirmed cardiomyopathy, and age-matched controls collected retrospectively from a study conducted at the University of Nebraska Medical Center in Omaha, Nebraska, USA. Subjects whose exam did not include at least one A2C, A3C, and A4C view each were excluded from the study cohort. The resulting 54-subject cohort included 4 patients with confirmed dilated cardiomyopathy (DCM), 16 patients with confirmed hypertrophic cardiomyopathy (HCM), and 34 age-matched controls (CTRL). Further information on the cohort demographics is provided in Table 1 and a breakdown of function indices is provided in Table 2.

A routine echocardiogram for each patient was performed on an iE33 ultrasound system (Philips Healthcare, Andover, MA, USA). All views were collected based on recommendations from the American Society of Echocardiograph [2]. Doppler-based measurements, provided in Table 2, were collected in the ALAX A4C view. Ventricle dimension measurements were computed using the Simpson bi-plane method on ALAX A4C and ALAX A2C views using the GE EchoPAC software. B-mode ALAX A2C, A3C, and A4C view scans were performed conventionally, as opposed to specifically collected for strain measurements. Images were stored in Digital Imaging and Communications in Medicine (DICOM) format for postprocessing.

A total of 900 individual heart beat records were analyzed, consisting of 573 control, 261 HCM, and 66 DCM from the 54-subjects. Peak absolute GLS, peak absolute systolic GLSr (GLS<sub>r</sub>), and peak absolute early diastolic GLSr (GLS<sub>r</sub><sub>e</sub>) for all measurement methods were computed. Data was classified into control and cardiomyopathy (CM) groups. Statistical significance was tested using Student's t-test between methods among the same condition as well as between each condition for each method. Receiver-operator curves (ROC) were computed for each quantified parameter across all views for all beats within each method. Area under the curve (AUC) was computed for each ROC curve. Additionally, statistical significance of GLS and GLS<sub>r</sub> was tested between the LTC method and each conventional GLS method.

## III. RESULTS

### A. Global longitudinal strain error analysis

Error analysis results are presented in Figure 2. The GLS<sub>r</sub> estimates (Figure 2a-1) by the DCC and FTC method yielded linear regression fits with similar slopes and bias of approximately  $m \approx 0.7\%$  and  $b \approx 0.025\%$ , and quality of fit of  $R_{DCC}^2=0.72$  and  $R_{FTC}^2=0.76$ . Conversely, LTC GLS<sub>r</sub> estimates had a slope fit of  $m = 0.92\%$  and bias of  $b = 0.016\%$  with a fit quality of  $R_{LTC}^2=0.85$ . Considering GLS<sub>r</sub> as a function of CNR (where values are normalized by  $GLS_r = 0.95s^{-1}$ ), shown in

Table 1: Demographics of study cohort for each disease state.

Characteristics	Control (n = 33)	DCM (n = 4)	HCM (n = 16)
Age (years)	17.98 ± 8.86	14.50 ± 6.24	18.74 ± 10.47
BSA (m <sup>2</sup> )	1.66 ± 0.56	1.52 ± 0.64	1.81 ± 0.69
Height (cm)	159.25 ± 29.11	147.90 ± 57.60	159.81 ± 30.86
Weight (kg)	63.50 ± 30.42	57.60 ± 35.65	75.71 ± 41.03
Heart Rate (bpm)	67.47 ± 17.26	92.50 ± 33.81	72.88 ± 18.78

Table 2: Indices for LV dimensions and functional parameters.

<i>Ventricular Dimensions</i>	Control (n = 33)	DCM (n = 4)	HCM (n = 16)
End Diastolic Volume (ml)	98.85 ± 39.19	178.75 ± 83.92	96.28 ± 37.66
End Systolic Volume (ml)	37.80 ± 15.84	117.75 ± 60.31	36.03 ± 18.40
Stroke Volume (ml)	61.29 ± 24.39	61.00 ± 33.32	59.44 ± 21.24
Ejection Fraction (%)	62.16 ± 3.50	34.25 ± 14.93	63.06 ± 6.01
<i>Functional Parameters</i>			
E-wave velocity (cm/s)	82.20 ± 19.70	102.25 ± 29.80	83.19 ± 19.59
A-wave velocity (cm/s)	42.84 ± 10.95	61.25 ± 34.74	61.13 ± 33.65
e' velocity (cm/s)	17.58 ± 3.22	11.38 ± 2.63	10.51 ± 3.04
E/A ratio	2.00 ± 0.59	2.24 ± 1.62	1.55 ± 0.50
E/e' ratio	4.06 ± 1.21	8.22 ± 4.30	7.34 ± 2.58

Figure 2a-2, the LTC method showed a 1.5 to 2-fold improvement in accuracy compared to DCC and a 1.5-fold improvement compared to FTC. Additionally, the error measurements suggest the LTC method is unaffected by CNR ( $MAE_{LTC}: 7.98\% - 8.58\%$ ;  $RMSE_{LTC}: 10.74\% - 11.33\%$ ). The FTC method also appears to be unaffected by CNR ( $MAE_{FTC}: 10.15\% - 10.85\%$ ;  $RMSE_{FTC}: 13.61\% - 14.42\%$ ), while the DCC method was noticeably affected by CNR ( $MAE_{DCC}: 10.54\% - 13.71\%$ ;  $RMSE_{DCC}: 14.83\% - 18.32\%$ ).

All GLS estimates by the DCC or FTC method maintained linear regression fits (Figure 2b-1) with similar slopes and biases of around  $m \approx 0.6$  and  $b \approx 0.3\%$ , and quality of fit of  $R_{DCC}^2=0.71$  and  $R_{FTC}^2=0.74$ . LTC GLS estimates show a slope of  $m = 0.92$  and bias of  $b = 0.09\%$  with a fit quality of  $R_{LTC}^2=0.91$ . The LTC method shows more than 200% improvement in measurement accuracy compared against the DCC and FTC methods as a function of CNR (Figure 2b-2), where values are normalized by  $GLS = 8.47\%$ . Again, the error analysis demonstrates the LTC method is unaffected by CNR ( $MAE_{LTC}: 6.12\% - 6.78\%$ ;  $RMSE_{LTC}: 8.33\% - 8.96\%$ ), and the DCC method is affected by signal quality ( $MAE_{DCC}: 13.62\% - 18.66\%$ ;  $RMSE_{DCC}: 18.84\% - 24.75\%$ ). Further, error measurements indicate the FTC

method GLS estimates are also affected by CNR ( $MAE_{FTC}$ : 13.07% – 16.00%;  $RMSE_{FTC}$ : 18.04% – 20.91%).

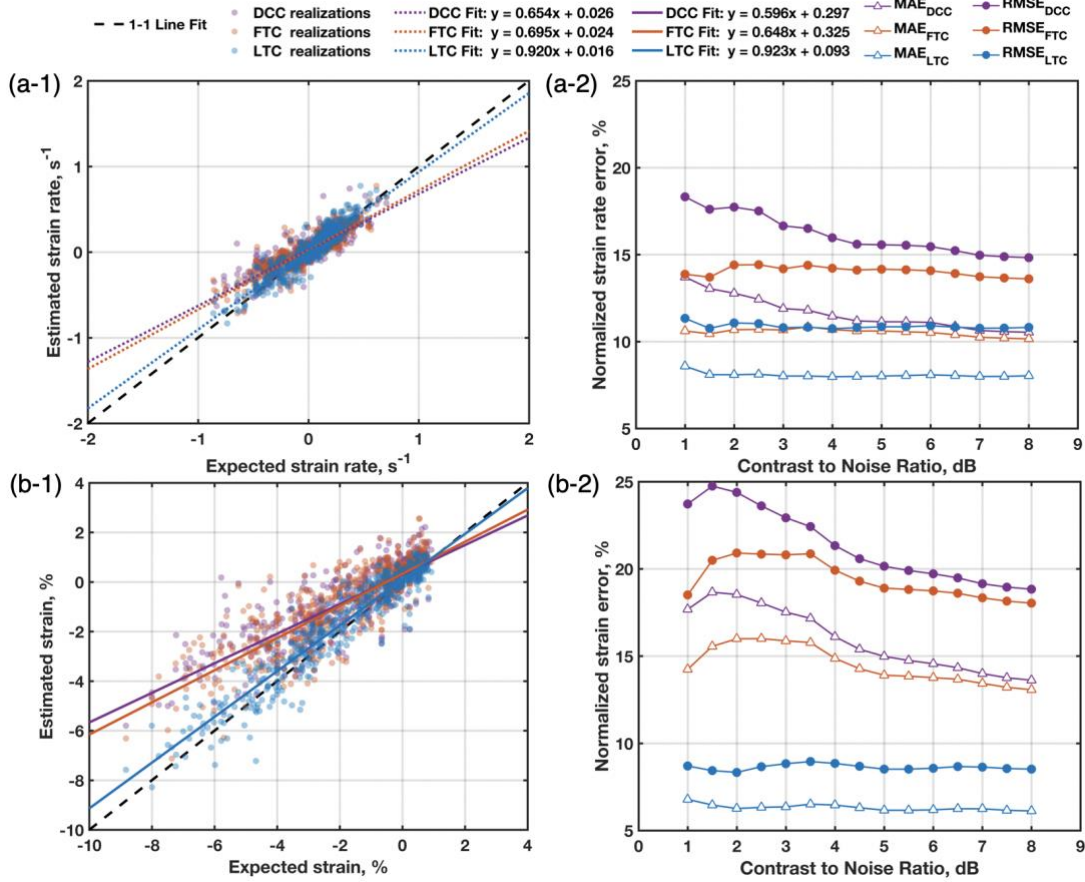


Figure 2: (Left) Direct comparison of measurements to ground truth values and (right) normalized error as a function of contrast-to-noise ratio (CNR) for (a) GLS and (b) GLSr quantities. Measurements were performed using the Direct Cross-Correlation method (DCC), Fourier Transform Correlation (FTC), and Fourier-based Logarithm Transform Correlation (LTC).

### B. Clinical imaging study

Results comparing the LTC method against conventional GLS methods for each parameter are presented in Figure 3a-1 thru 3c-1. LTC consistently resolved larger measurements of peak GLS ( $\overline{GLS}_{LTC,CTRL} = 15.83\%$ ,  $\overline{GLS}_{LTC,CM} = 10.50\%$ ), GLSrs ( $\overline{GLSre}_{LTC,CTRL} = 0.73s^{-1}$ ,  $\overline{GLSre}_{LTC,CM} = 0.55s^{-1}$ ), and GLSre ( $\overline{GLS}_{LTC,CTRL} = 1.30s^{-1}$ ,  $\overline{GLS}_{LTC,CM} = 0.66s^{-1}$ ) compared to the conventional methods. FTC mean peak GLS measurements ( $\overline{GLS}_{FTC,CTRL} = 9.03\%$ ,  $\overline{GLS}_{FTC,CM} = 5.80\%$ ) were slightly increased compared to the DCC mean peak GLS ( $\overline{GLS}_{DCC,CTRL} = 7.90\%$ ,  $\overline{GLS}_{DCC,CM} = 5.10\%$ ); however the FTC maintained a larger variance across both health states. This occurred for FTC GLSre and GLSrs ( $\overline{GLSre}_{FTC,CTRL} = 0.73s^{-1}$ ,  $\overline{GLSre}_{FTC,CM} = 0.42s^{-1}$ ;  $\overline{GLSre}_{FTC,CTRL} = 0.51s^{-1}$ ,  $\overline{GLSre}_{FTC,CM} = 0.37s^{-1}$ ). Similar results were seen for the DCC method as well ( $\overline{GLSre}_{DCC,CTRL} = 0.59s^{-1}$ ,  $\overline{GLSre}_{DCC,CM} = 0.36s^{-1}$ ;  $\overline{GLSre}_{DCC,CTRL} =$

$0.47s^{-1}$ ,  $\overline{GLSre}_{DCC,CM} = 0.34s^{-1}$ ). Statistical significance tests indicated the group means were statistically significant ( $p < 0.001$  for all cases except between FTC and DCC CM, which was  $p < 0.05$ ).

ROC curves for each GLS parameter using each method are presented in Figure 3a-2 thru 3c-2. Results from the peak GLS ROC curves (Figure 3a-2) show that the LTC method AUC was 0.85, while the FTC and DCC AUCs were near 0.75. Peak GLSrs ROC curves (Figure 3b-2) show that all methods performed similarly in detecting abnormal function for this dataset. The LTC had  $p < 0.05$  when compared to FTC but showed weak significance to DCC. Finally, for the peak GLSre ROC curves (Figure 3c-2), the LTC maintained an AUC of 0.82 and FTC method had an AUC of 0.75, but both methods did not achieve the AUC from the peak GLS. Additionally, LTC achieved  $p < 0.05$  against both methods.

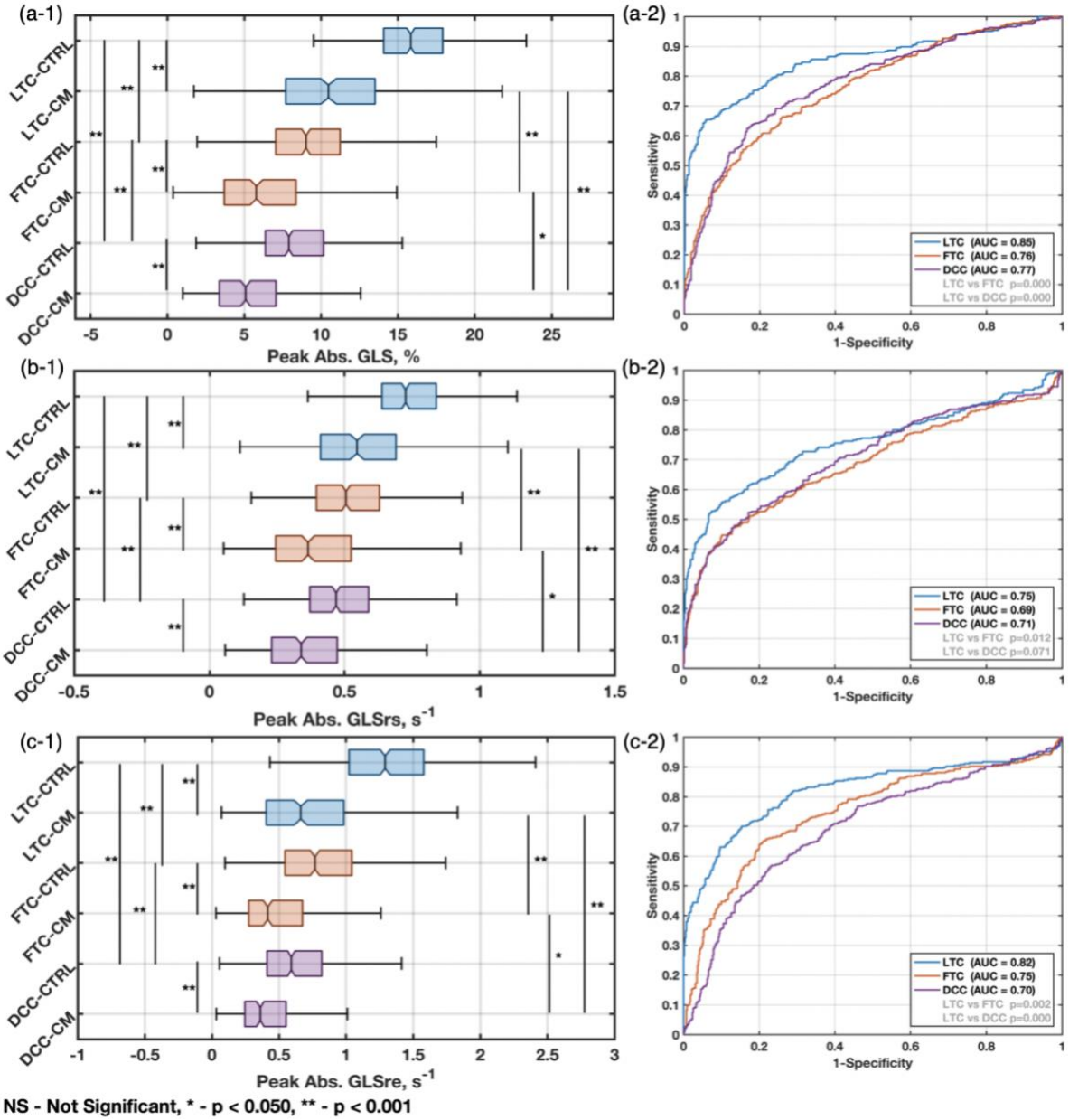


Figure 3: Distribution of measurements and significance tests for each GLS measurement method on observing (a-1) peak absolute GLS, (b-1) peak absolute systolic GLSr, and (c-1) peak absolute diastolic GLSr. (2) Receiver-operator curves displaying the ability for the LTC method estimated parameters to distinguish between normal and abnormal cardiac disease states based on (a-2) peak absolute GLS, (b-2) peak absolute systolic GLSr, and (c-2) peak absolute diastolic GLSr.

#### IV. DISCUSSION

This study presents a new algorithm, the LTC method, for computing GLS and GLSr estimates from ultrasound scans. Error analysis using synthetic ultrasound images were presented to demonstrate and quantify the LTC method's improvement over current methods, and a clinical cohort was analyzed using all methods. The LTC method does not rely on any shape assumptions of the LV, avoids the use of boundary segmentation, and enables reliable determination of GLS and GLSr measurements even when a small portion of the LV may be clipped, drops out, or is obscured by noise artifacts. Furthermore, because LV segmentation is not required, regularization to preserve the segmentation shape during tracking is avoided.

The LTC method offers a unique approach by computing the “displacement of the gradients” or the GLSr between sequential frames in the time series. By obtaining GLSr, we can ensure a reliable rate measurement. Computing GLS through the GLSr provides a smoothing operation to suppress noise. Commercial platforms that calculate GLS have built-in constraints that enforce tracked boundaries to be smooth in space and time, providing measurements may appear physically consistent, but to a degree are also driven by the regularization functions used. When GLSr is computed, error due to regularization may require further data correction.

##### A. Synthetic ultrasound recordings

The error analysis presented in Figure 2 demonstrated a dependence of the DCC method on CNR. This result was expected due to spatial CC kernel relying on individual pixel



intensities. As CNR approaches 1, the mean pixel intensity of the myocardial fiber speckle data and mean pixel intensity of speckle noise in the LV are equivalent. This means the speckle noise cannot be differentiated from the myocardial wall, making the physical features ambiguous for the DCC method. The FTC method is less affected by low CNR because the spectral CC kernel correlates the speckle features, meaning the kernel is less susceptible to observing large non-physical erroneous measurements when speckle noise is present with respect to the spatial CC kernel. However, the spectral CC kernel will tend to estimate near-zero displacements with low CNR. Both kernels are used in computing GLS but results are underestimated, possibly suggesting avoidance of GLS computation using these methods all together as indicated by [1]. The LTC method enables GLS computation with suboptimal images that still provide reliable measurements, comparable to optimal image findings, reflected by the MAE and RMSE plots in Figure 2.

### B. Clinical study

Comparison of each method for all disease conditions, presented in Figure 3a-1, b-1, and c-1, presented the distribution of measurements and their statistical significance. Within each method the CTRL and CM distributions showed overlap while the significance tests indicated each group mean came from an independent distribution. Between methods, the LTC method reported larger GLS and GLSr values compared to the conventional algorithms, while the conventional methods were reported similarly between each other. Again, statistical significance was reported between methods, while distributions showed at least some overlap. Comparison results suggest normal function would report larger GLS and GLSr values compared to abnormal function but establishing improvement of the LTC method through this analysis alone may not be possible. For this reason, the ROC curves, presented in Figure 3a-2, 3b-2, and 3c-2, are used to determine if clinical separation is possible. The peak GLS and GLSre ROC curves show a 10% improvement in classification, which would enable an observable improvement in the rate of correct diagnosis (conventional methods showed 3 in every 4 patients correctly diagnosed, while LTC offered more than 4 in every 5 patients being correctly diagnosed from the current dataset).

Several factors from the data caused the spatial and spectral CC kernels to fail. First, echocardiogram quality in some scans was not optimal for conventional algorithms, depicting shadows, poor signal, respiration, and pixel intensity saturation. Further, some subjects were children under the age of 10 ( $n = 11$ ) with smaller hearts and higher heart rates and may have had trouble holding still through the imaging study. These subjects provide scans with lower spatial resolution and temporal resolution, which are known to contribute to CC failure. Implementation differences between the FTC, DCC, and LTC methods can lead to additional discrepancies in GLS measurements. For the FTC and DCC methods, discrepancies can arise from tracking an over-smoothed boundary. In the case of the LTC method, the kernel provides a “most probable”

GLSr value for each frame; small errors in GLSr will propagate into the GLS integration.

LTC peak GLSre measurements were in agreement with literature (peak GLSre  $> 1s^{-1}$ ) (Morris et al 2017), while GLS and GLSrs measurements consistently fell below nominal ranges from literature (peak GLS  $> 18\%$ ; peak GLSrs  $> 1s^{-1}$ ) (Jashari et al 2015). For the LTC algorithm, this underestimation was potentially the result of the averaging that occurs in the correlation estimate which can bias measurements below their true value. Commercial methods rely on significant regularization steps which force the measurements to fit LV shape models and functions [1], [15], thereby shaping the GLS measurements as a function of regularization instead of the true underlying deformation, feasibly elevating values.

### C. Limitations

The LTC method makes several assumptions that will require further validation. The algorithm assumes that GLS and GLSr can be reliably measured from the septal and lateral walls, ignoring shortening that occurs near the apex. In some DCM cases, where GLS and GLSr values are small, the LTC kernel obtains measurements that may have greater uncertainty. Further, the algorithm assumes reorientation has been performed correctly and no misalignment is present. If a scan is misaligned, the algorithm may provide measurements which are not purely GLS, but a combination of GLS and off-axis strain.

The clinical validation in this study was performed on pediatric data. This set proved challenging for conventional GLS methods to work properly. One subject classified with HCM presented measurements that consistently agreed with measurements reported in the CTRL group. An additional five HCM subjects and two DCM subjects had E/e' and LV relaxation that compared similarly to the CTRL group. In these 8 subjects, the disease characteristics appear more mild and closer to normal cardiac function. Although this enabled us to demonstrate the power of the LTC method, a dataset optimized for GLS estimation would help further substantiate findings. Additionally, validation of this technique should be performed beyond pediatric subjects. Strain-based decision making is becoming more common in adult heart failure. More rigorous validation should also be performed against commercially available state-of-the art technologies such as TomTec AutoStrain and GE EchoPAC.

## V. CONCLUSION

Clinical decision making with GLS measurements has emerged as a means of studying patient cardiac function. However, the use of this technology is limited by factors which narrow application, require expertise, and force clinics to analyze patients with the same software because industry standards do not exist. In this work we present a new method, the LTC method, for determining GLS and GLSr measurements from ultrasound scans. The LTC method does not require shape assumptions, is machine-agnostic, and limits heuristic inputs. We compared the LTC method against conventional GLS

algorithms with the use of synthetic ultrasound scans, analyzing error from the ground truth GLS and GLSr, and validated using clinical data from a study of pediatric cardiomyopathies. Results showed this method is unaffected by image quality, providing reliable results over a wide range of image quality values. Furthermore, the proposed method showed a 200% improvement in measurement accuracy against conventional methods for both the synthetic data and clinical cohort. Our LTC technique should be viewed as an initial approach to obtaining GLS measurements from clinical scans by virtue of the methods improved capabilities in analyzing suboptimal image quality recordings.

#### ACKNOWLEDGEMENTS

The authors would like to thank Mary J. Craft for her time and effort in data collect, aggregation, and sharing between universities.

#### REFERENCES

- [1] R. M. Lang et al., "Recommendations for cardiac chamber quantification by echocardiography in adults: an update from the American Society of Echocardiography and the European Association of Cardiovascular Imaging," *Eur. Hear. Journal-Cardiovascular Imaging*, vol. 16, no. 3, pp. 233–271, 2015.
- [2] L. Lopez et al., "Recommendations for quantification methods during the performance of a pediatric echocardiogram: a report from the Pediatric Measurements Writing Group of the American Society of Echocardiography Pediatric and Congenital Heart Disease Council," *J. Am. Soc. Echocardiogr.*, vol. 23, no. 5, pp. 465–495, 2010.
- [3] V. Zacà, P. Ballo, M. Galderisi, and S. Mondillo, "Echocardiography in the assessment of left ventricular longitudinal systolic function: current methodology and clinical applications," *Heart Fail. Rev.*, vol. 15, no. 1, p. 23, 2010.
- [4] K. Dickstein et al., "ESC Guidelines for the diagnosis and treatment of acute and chronic heart failure 2008: The Task Force for the Diagnosis and Treatment of Acute and Chronic Heart Failure 2008 of the European Society of Cardiology. Developed in collaboration with the Heart," pp. 933–989, 2008.
- [5] K. Dickstein et al., "ESC Guidelines for the diagnosis and treatment of acute and chronic heart failure 2008," *Eur. J. Heart Fail.*, vol. 10, no. 10, pp. 933–989, 2014.
- [6] P. Ponikowski et al., "2016 ESC Guidelines for the diagnosis and treatment of acute and chronic heart failure: The Task Force for the diagnosis and treatment of acute and chronic heart failure of the European Society of Cardiology (ESC). Developed with the special contribution," *Eur. J. Heart Fail.*, vol. 18, no. 8, pp. 891–975, 2016.
- [7] H. Nesser and S. Winter, "Speckle tracking in the evaluation of left ventricular dyssynchrony," *Echocardiography*, vol. 26, no. 3, pp. 324–336, 2009.
- [8] R. Hoffmann et al., "Analysis of left ventricular volumes and function: a multicenter comparison of cardiac magnetic resonance imaging, cine ventriculography, and unenhanced and contrast-enhanced two-dimensional and three-dimensional echocardiography," *J. Am. Soc. Echocardiogr.*, vol. 27, no. 3, pp. 292–301, 2014.
- [9] O. A. Smiseth, H. Torp, A. Opdahl, K. H. Haugaa, and S. Urheim, "Myocardial strain imaging: how useful is it in clinical decision making?," *Eur. Heart J.*, vol. 37, no. 15, pp. 1196–1207, 2016.
- [10] B. H. Amundsen et al., "Noninvasive Myocardial Strain Measurement by Speckle Tracking Echocardiography," *J. Am. Coll. Cardiol.*, vol. 47, no. 4, pp. 789–793, 2006.
- [11] T. Helle-Valle et al., "New noninvasive method for assessment of left ventricular rotation: speckle tracking echocardiography," *Circulation*, vol. 112, no. 20, pp. 3149–3156, 2005.
- [12] H. Blessberger and T. Binder, "Two dimensional speckle tracking echocardiography: basic principles," *Heart*, vol. 96, no. 9, pp. 716–722, 2010.
- [13] A. Rösner, D. Barbosa, E. Aarsæther, D. Kjønnås, H. Schirmer, and J. D'hooge, "The influence of frame rate on two-dimensional speckle-tracking strain measurements: a study on silico-simulated models and images recorded in patients," *Eur. Hear. Journal-Cardiovascular Imaging*, vol. 16, no. 10, pp. 1137–1147, 2015.
- [14] M. Leitman et al., "Circumferential and longitudinal strain in 3 myocardial layers in normal subjects and in patients with regional left ventricular dysfunction," *J. Am. Soc. Echocardiogr.*, vol. 23, no. 1, pp. 64–70, 2010.
- [15] J. U. Voigt et al., "Definitions for a common standard for 2D speckle tracking echocardiography: consensus document of the EACVI/ASE/Industry Task Force to standardize deformation imaging," *Eur. Hear. J. - Cardiovasc. Imaging*, vol. 16, no. 1, pp. 1–11, 2015.
- [16] K. E. Farsalinos, A. M. Daraban, S. Ünlü, J. D. Thomas, L. P. Badano, and J.-U. U. Voigt, "Head-to-Head Comparison of Global Longitudinal Strain Measurements among Nine Different Vendors: The EACVI/ASE Inter-Vendor Comparison Study," *J. Am. Soc. Echocardiogr.*, vol. 28, no. 10, pp. 1171–1181.e2, 2015.
- [17] K. Kalam, P. Otahal, and T. H. Marwick, "Prognostic implications of global LV dysfunction: a systematic review and meta-analysis of global longitudinal strain and ejection fraction," *Heart*, vol. 100, no. 21, pp. 1673–1680, 2014.
- [18] T. Yingchoncharoen, S. Agarwal, Z. B. Popović, and T. H. Marwick, "Normal Ranges of Left Ventricular Strain: A Meta-Analysis," *J. Am. Soc. Echocardiogr.*, vol. 26, no. 2, pp. 185–191, 2013.
- [19] M. E. Menting et al., "Normal myocardial strain values using 2D speckle tracking echocardiography in healthy adults aged 20 to 72 years," *Echocardiography*, vol. 33, no. 11, pp. 1665–1675, 2016.

- [20] M. Alessandrini et al., “Realistic Vendor-Specific Synthetic Ultrasound Data for Quality Assurance of 2-D Speckle Tracking Echocardiography: Simulation Pipeline and Open Access Database,” *IEEE Trans. Ultrason. Ferroelectr. Freq. Control*, vol. 65, no. 3, pp. 411–422, 2018.
- [21] P. E. Anuta, “Spatial registration of multispectral and multitemporal digital imagery using fast fourier transform techniques,” *IEEE Trans. Geosci. Electron.*, vol. ge-8, no. 4, p. 353, 1970.
- [22] L. N. Bohs and G. E. Trahey, “A Novel Method for Angle Independent Ultrasonic Imaging of Blood Flow and Tissue Motion,” *IEEE Trans. Biomed. Eng.*, vol. 38, no. 3, pp. 1–7, 1991.
- [23] M. O’Donnell, A. R. Skovoroda, B. M. Shapo, and S. Y. Emelianov, “Internal Displacement and Strain Imaging Using Ultrasonic Speckle Tracking,” *IEEE Trans. Ultrason. Ferroelectr. Freq. Control*, vol. 41, no. 3, pp. 314–325, 1994.
- [24] C. E. Willert and M. Gharib, “Digital Particle Image Velocimetry,” *Exp. Fluids*, vol. 10, no. 4, pp. 181–193, 1991.
- [25] T. C. Chu, W. F. Ranson, M. a Sutton, and W. H. Peters, “Applications of Digital Image Correlation Techniques to Experimental Mechanics,” *Exp. Mech.*, vol. 25, no. September, pp. 232–244, 1985.
- [26] H. A. Bruck, S. R. McNeill, M. A. Sutton, and W. H. Peters III, “Digital Image Correlation Using Newton-Raphson Method of Partial Differential Correction,” *Exp. Mech.*, vol. 29, no. 3, pp. 261–267, 1989.
- [27] R. N. Bracewell, K.-Y. Chang, A. K. Jha, and Y.-H. Wang, “Affine theorem for two-dimensional Fourier transform,” *Electron. Lett.*, vol. 29, no. 3, p. 1, 2016.
- [28] Q. sheng Chen, M. Defrise, and F. Deconinck, “Symmetric Phase-Only Matched Filtering of Fourier-Mellin Transforms for Image Registration and Recognition,” *IEEE Trans. Pattern Anal. Mach. Intell.*, vol. 16, no. 12, pp. 1156–1168, 1994.
- [29] M. N. Giarra, J. J. Charonko, and P. P. Vlachos, “Measurement of fluid rotation, dilation, and displacement in particle image velocimetry using a Fourier-Mellin cross-correlation,” *Meas. Sci. Technol.*, vol. 26, no. 3, pp. 1–11, 2015.
- [30] B. S. Reddy and B. N. Chatterji, “An FFT-based technique for translation, rotation, and scale-invariant image registration,” *IEEE Trans. image Process.*, vol. 5, no. 8, pp. 1266–1271, 1996.
- [31] A. Eckstein and P. P. Vlachos, “Assessment of advanced windowing techniques for digital particle image velocimetry (DPIV),” *Meas. Sci. Technol.*, vol. 20, no. 7, p. 075402, 2009.
- [32] B. A. Meyers, C. J. Goergen, and P. P. Vlachos, “Development and Validation of a Phase-Filtered Moving Ensemble Correlation for Echocardiographic Particle Image Velocimetry,” *Ultrasound Med. Biol.*, vol. 44, no. 2, pp. 477–488, 2018.
- [33] A. Eckstein and P. P. Vlachos, “Digital particle image velocimetry (DPIV) robust phase correlation,” *Meas. Sci. Technol.*, vol. 20, no. 5, p. 055401, 2009.
- [34] A. C. Eckstein, J. Charonko, and P. Vlachos, “Phase correlation processing for DPIV measurements,” *Exp. Fluids*, vol. 45, no. 3, pp. 485–500, 2008.
- [35] M. Alessandrini et al., “Generation of ultra-realistic synthetic echocardiographic sequences to facilitate standardization of deformation imaging,” in *2015 IEEE 12th International Symposium on Biomedical Imaging (ISBI)*, 2015, vol. 2015-July, no. September, pp. 756–759.
- [36] J. D. Thomas and L. P. Badano, “EACVI-ASE-industry initiative to standardize deformation imaging: a brief update from the co-chairs,” *Eur. Hear. J. - Cardiovasc. Imaging*, vol. 14, no. 11, pp. 1039–1040, 2013.
- [37] J. D’hooge et al., “Two-dimensional speckle tracking echocardiography: standardization efforts based on synthetic ultrasound data,” *Eur. Hear. Journal-Cardiovascular Imaging*, vol. 17, no. 6, pp. 693–701, 2015.
- [38] O. Mirea et al., “Intervendor differences in the accuracy of detecting regional functional abnormalities: a report from the EACVI-ASE Strain Standardization Task Force,” *JACC Cardiovasc. Imaging*, vol. 11, no. 1, pp. 25–34, 2018.
- [39] O. Mirea et al., “Variability and reproducibility of segmental longitudinal strain measurement: a report from the EACVI-ASE Strain Standardization Task Force,” *JACC Cardiovasc. Imaging*, vol. 11, no. 1, pp. 15–24, 2018.
- [40] M. Alessandrini et al., “A pipeline for the generation of realistic 3D synthetic echocardiographic sequences: Methodology and open-access database,” *IEEE Trans. Med. Imaging*, vol. 34, no. 7, pp. 1436–1451, 2015.
- [41] M. A. L. Bell, R. Goswami, J. A. Kisslo, J. J. Dahl, and G. E. Trahey, “Short-lag spatial coherence imaging of cardiac ultrasound data: Initial clinical results,” *Ultrasound Med. Biol.*, vol. 39, no. 10, pp. 1861–1874, 2013.